

# Unraveling microforging principle during in situ shot-peening-assisted cold spray additive manufacturing aluminum alloy through a multi-physics framework

Qian Wang <sup>a,\*</sup>, Ninsuh Ma <sup>a,\*</sup>, Junmiao Shi <sup>b</sup>, Wenjia Huang <sup>a</sup>, Xiao-Tao Luo <sup>c,\*</sup>, Peihao Geng <sup>a</sup>, Mingxing Zhang <sup>d</sup>, Xian-Cheng Zhang <sup>b</sup>, Chang-Jiu Li <sup>c</sup>

<sup>a</sup> Joining and Welding Research Institute, Osaka University, Osaka 567-0047, Japan

<sup>b</sup> Key Laboratory of Pressure Systems and Safety, Ministry of Education, East China University of Science and Technology, Shanghai 200237, China

<sup>c</sup> State Key Laboratory for Mechanical Behavior of Materials, School of Materials Science and Engineering, Xi'an Jiaotong University, Xi'an, Shaanxi 710049, China

<sup>d</sup> Division of Materials, School of Engineering, University of Queensland, St Lucia, Brisbane, Qld 4072, Australia



## ARTICLE INFO

### Keywords:

Cold spray  
Additive manufacturing  
Extreme deformation  
Grain refinement  
Microforging

## ABSTRACT

Cold spray (CS) is a highly potential solid-state additive manufacturing (AM) technique. In situ shot-peening-assisted CSAM was proposed to additively manufacture fully dense deposits using cost-effective and renewable nitrogen gas. The role of in situ shot-peening particles is critical but remains unclear. Here, the process was quantitatively modeled to visualize the dynamic deformation, energy conversion, as well as cell/sub-grain size and microhardness evolutions, compared to those during the conventional CSAM process, identifying the key role of in situ shot-peening particles in the AA6061 extreme deformation and microstructure characteristics during in situ shot-peening-assisted CSAM. High-fidelity modeling was verified fully by comparing the experimental and model-reproduced deformation profiles, cell/sub-grain size distributions, and increases in microhardness. The results show that the kinetic energy of in situ shot-peening particles was 470 times higher and dissipated mainly through AA6061 plastic deformation (86.36% of total energy), leading to significant enhancement of microhardness and tensile strength. Moreover, the mixing ratio of large-size SS410 particles required to create a fully dense deposit was evaluated from an energy perspective, in good agreement with the experiment. This study elucidates the microforging principle during in situ shot-peening-assisted CSAM, providing scientific guidelines for high-quality and low-cost CSAM of high-strength aluminum alloys.

## 1. Introduction

Additive manufacturing (AM) is an umbrella term for techniques that stack materials on top of each other to create entities. It is flourishing owing to the remarkable design flexibility [1–3]. For the AM of metallic materials, various fusion-based AM techniques (e.g., direct laser deposition [4–6], wire arc AM [7,8], and electron beam melting [9]) that directly build parts or components through the layer-upon-layer melting and solidification of metals have been initiated and researched extensively within the past decades. Metal melting ensures reliable bonding among layers; however, the rapid solidification tends to induce noticeable thermal stress/deformation/cracking [4,6,8,10,11], element segregation/oxidation/evaporation [4,9,11–13], grain growth/coarsening [4,7,14,15], phase transformation [4,11,16], etc. The advent of

cold spray (CS) signals a new direction. Supersonic impact of metallic microparticles (generally  $400\text{--}1200 \text{ m}\cdot\text{s}^{-1}$  [17]) enables solid-state deposition, minimizing the above solidification-related issues and even allowing the deposition of high-laser-reflectivity, nano-, or amorphous materials. Originally discovered for spraying, it evolved into a representative solid-state AM technique (written in the ASTM F2792-12A standard [18,19]) due to the unlimited build-up dimensions. Moreover, the advantages of immense deposition rate [20,21], feedstock reusability [22], and environmental friendliness [23] make CSAM attract considerable attention from academia and industry.

CSAM is highly promising, but it is noteworthy that the deposition quality depends largely on the plastic deformation capacity of metallic microparticles. Take aluminum materials as an example. Highly dense pure Al CSAM deposits can be obtained conveniently because of the low

\* Corresponding authors.

E-mail addresses: [wang.qian.jwri@osaka-u.ac.jp](mailto:wang.qian.jwri@osaka-u.ac.jp) (Q. Wang), [ma.ninshu.jwri@osaka-u.ac.jp](mailto:ma.ninshu.jwri@osaka-u.ac.jp) (N. Ma), [luoxiaotao@xjtu.edu.cn](mailto:luoxiaotao@xjtu.edu.cn) (X.-T. Luo).

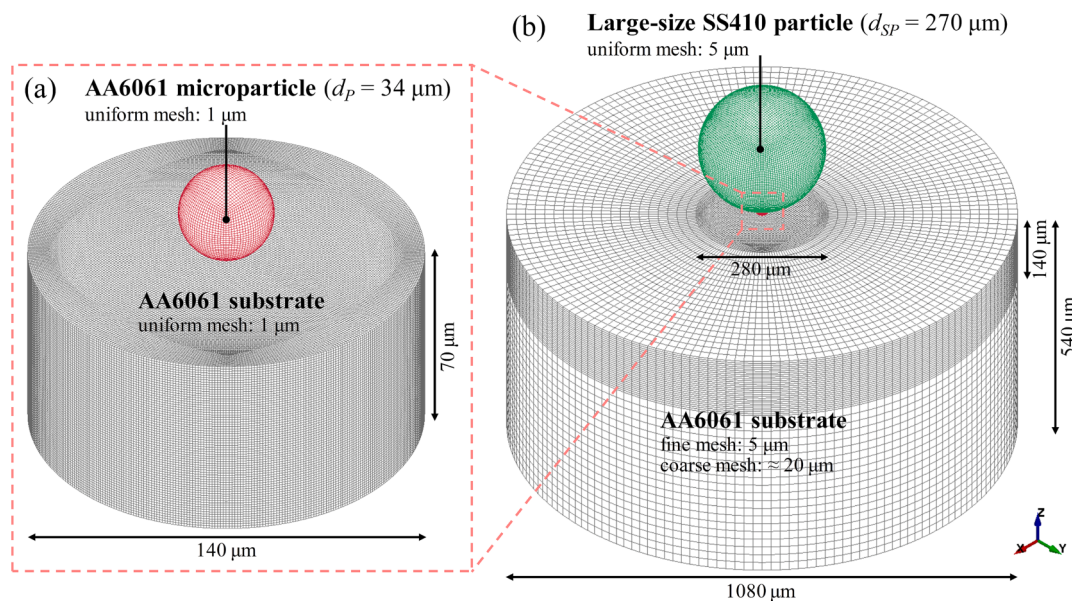


**Fig. 1.** Geometric dimensions and meshing for simulating the supersonic impact processes of AA6061 microparticles on AA6061 substrates (a) without and (b) with in situ shot-peening, based on experiments.

strength and, thus, good deformability [24–26]. Today, the AM market for high-performance Al alloys (e.g., 2xxx, 6xxx, and 7xxx series) is growing rapidly, especially in response to the increasing demand for lightweight structures in transportation infrastructures (e.g., automobiles and aircrafts) to meet “sustainable development goals” (SDGs) and carbon neutrality. Their fusion-based AM encounters intolerable solidification defects including columnar grains and cracking, and the re-alloy design of microparticles is imperative [27–30]. CSAM opens up a new space for AM using existing high-performance Al alloys but has the issue of a high porosity resulting from the insufficient deformation of microparticles [31–36]. Increasing the impact velocity and temperature of microparticles themselves is commonly applied to promote deformation, but this places high demands on the accelerating gas (generally expensive and non-renewable helium [31,32,34,36–38]) and CSAM equipment [39,40]. Meticulously promoting deformation is of great importance. An effective strategy is to introduce external forces.

During CSAM, the larger the particle size, the lower the impact velocity [41–43]. A low impact velocity allows the particles to rebound after impact, i.e., shot peening. Large-size particles bring additional kinetic energy to assist deformation (namely microforging) but are not deposited. Therefore, we proposed in situ shot-peening-assist CSAM as an improved CSAM method. The essence is a mixture of small-size (used for deposition) and large-size (used for in situ shot-peening) particles. Crucially, this method does not require equipment upgrading, and, helpfully, the injection of shot-peening particles can prevent nozzle clogging. Preliminary experiments have demonstrated the feasibility [43,44–47]. Highly dense deposits with uniform ultra-fine grains can also be produced for hard-to-deform materials using low-cost, renewable nitrogen as the accelerating gas. Nevertheless, lacking explicit knowledge of materials with non-linear, non-equilibrium, and high strain-rate responses deprives scientific means to optimize the process. Microballistic testing enables real-time observation of single-particle supersonic impacts [42,48–50]. Still, the detailed information on stress/strain/strain-rate/temperature, energy conversion, microstructure evolution, and correlation with mechanical properties remain unknowable, inhibiting the understanding of the process. Thus, quantitative modeling is imperative to understand the process fully and, especially, the key role of in situ shot-peening particles.

The purpose of this paper is to present a scientific strategy for understanding the material response behavior during in situ shot-peening-

assisted CSAM, focusing on the key role of in situ shot-peening particles. Crucially, a multi-physics modeling was developed based on dislocation dynamics, and the model accuracy was validated experimentally. The dynamic deformation, energy conversion, as well as cell/sub-grain size and microhardness evolutions during the process were reproduced for direct comparison with those during conventional CSAM, illustrating the microforging principle during in situ shot-peening-assisted CSAM. On this basis, the mixing ratio of in situ shot-peening particles required to form a fully dense deposit with uniform ultra-fine grains was correctly estimated in terms of energy, indicating the potential of the proposed model in guiding in situ shot-peening-assisted CSAM process optimization.

## 2. Materials and experiments

The target material was set as aluminum alloy 6061 (AA6061), a representative high-performance aluminum alloy having broad applications. Gas-atomized AA6061 microparticles with an average diameter of 34 μm ( $d_p = 34 \mu\text{m}$ ) and good sphericity were deposited using CSAM. Stainless steel 410 (SS410) particles, the industrial reference media for shot peening, having large size ( $d_{SP} = 270 \mu\text{m}$ ), good sphericity, high hardness (390 HV<sub>0.05</sub>, much harder to deform than AA6061), and high toughness, were chosen for in situ shot-peening in the CSAM described above. Large-size SS410 particles are inexpensive and easy to purchase commercially. In addition, they are magnetic, which enables easy recycling using an electromagnetic device; this is consistent with SDGs. During in situ shot-peening-assisted CSAM, the larger the particle size, the lower the particle impact velocity, but the lower the critical impact velocity required for deposition [42,43]. To minimize the contamination issue associated with in situ shot-peening, the high hardness of the large-size SS410 particles ensures almost no deformation during in situ shot-peening-assisted CSAM and, thus, no deposition or fragmentation. AA6061 sheets of 100 × 50 × 10 mm<sup>3</sup> were used as substrates after grinding, polishing, and ultrasonic cleaning. Large-size SS410 particles were ultrasonically cleaned to minimize contamination.

In situ shot-peening-assisted CSAM was implemented by premixing AA6061 microparticles and large-size SS410 particles, using inexpensive and renewable nitrogen as the accelerating gas. For comparison, the corresponding conventional CSAM was also carried out. The average impact velocities of AA6061 microparticles and large-size SS410

particles during the processes were  $500 \text{ m}\cdot\text{s}^{-1}$  and  $285 \text{ m}\cdot\text{s}^{-1}$ , respectively, as measured by an on-line diagnostic system of in-flight particles (DPV-2000 system, TECNAR Automation Ltd., Canada). Their average impact temperatures were estimated by a conventional computational fluid dynamic simulation to be  $75^\circ\text{C}$  and  $25^\circ\text{C}$ , while the substrate temperature was  $25^\circ\text{C}$ . Deposit microstructures were characterized using a high-precision field-emission scanning electron microscope (FE-SEM, Hitachi, Ltd., Japan) equipped with an EBSD system (TSL Co., Ltd., Japan) for subsequent model validation. To expose the interparticle interfaces, the polished deposits were subjected to 40 s etching using Keller's reagent. Microhardness was measured by an automatic micro-indentation tester (HM-221, Mitutoyo Corp., Japan) with a load of 50 g for 15 s to evidence the microstructure-performance relationship. Tensile testing was performed with reference to ISO 6892-1 standard, and the specimens were cut to  $62 \times 12 \times 1 \text{ mm}^3$  (gauge length 20 mm and center width 5 mm) by wire electrical discharge machining.

### 3. Numerical framework

#### 3.1. Geometric modeling

Ideally, the entire processes of in situ shot-peening-assisted CSAM and conventional CSAM with detailed deformation and microstructure evolution are accurately reproduced by numerical simulations. For now, however, it is nearly impossible. First, the process involves numerous particles impacting at high velocities, and the computational complexity is incalculable. Second, it is incredibly difficult to match the particle size, position, velocity, and angle distributions with reality. In general, it is universally recognized as more appropriate to extract key factors with statistical data for modeling [51–55]. Herein, the key to modeling was to elucidate the microforging principle during in situ shot-peening-assisted CSAM. Thus, two basic models based on experiments (Fig. 1) were developed to identify the key role of in situ shot-peening particles. Fig. 1a describes an AA6061 microparticle impacting itself during conventional or in situ shot-peening-assisted CSAM. The AA6061 microparticle was set as a sphere of  $34 \mu\text{m}$  diameter ( $d_p = 34 \mu\text{m}$ ) for realism. The AA6061 substrate was assumed to be a cylinder with a radius and height of  $70 \mu\text{m}$  ( $r/h \approx 2 d_p$ ), and its lateral and bottom surfaces were set as non-reflecting boundaries to eliminate the interference of error waves and to guarantee the high accuracy of simulations (see Section 4.1 for validation). Both were divided by a nominal mesh size of  $1 \mu\text{m}$  ( $d_p/34$ , validated in our previous study [56]) to capture details accurately. A mesh convergence analysis is appended in Supplementary Note S1. On this basis, the basic model (Fig. 1b) was constructed to identify the critical role of in situ shot-peening. The AA6061 microparticle was still created as a  $34 \mu\text{m}$  diameter ( $d_p = 34 \mu\text{m}$ ) sphere with  $1 \mu\text{m}$  nominal meshes. The large-size SS410 particle was set as a  $270 \mu\text{m}$  diameter ( $d_{sp} = 270 \mu\text{m}$ ) sphere for realism, and the substrate was assumed to be a cylinder with  $540 \mu\text{m}$  radius and height ( $r/h \approx 16 d_p$  or  $2 d_{sp}$ ). Meshing is particularly important considering the large size differences. Both the large-size SS410 particle and the center impact region ( $r/h \approx 140 \mu\text{m}$ ) of the AA6061 substrate, of interest, were divided by a nominal mesh size of  $5 \mu\text{m}$  ( $d_{sp}/54$ ) to ensure high accuracy, and the substrate remaining region was divided into  $\sim 20 \mu\text{m}$  coarse meshes to save computation costs. To identify the critical role of in situ shot-peening, it is essential that the mesh size consistency between the large-size SS410 particle and substrate in Fig. 1b. The boundary setting was identical to Fig. 1a. Similarly, multi-particle impact models without and with in situ shot-peening were built and not detailed here.

#### 3.2. Material and microstructure modeling

Within both CSAM processes, AA6061 microparticles and substrates were subjected to extreme deformation over wide-range strain rates (up to  $10^8 \text{ s}^{-1}$ ) with localized temperature rise. We developed the Ma-Wang (MW) material model using dislocation dynamics earlier, and its

**Table 1**

Parameters of AA6061 used for the MW material model, and those of SS410 used for the elastic-perfectly plastic material model.

(AA6061) MW material model	(SS410) Elastic-perfectly plastic material model	Parameters
Young's modulus $E$ (GPa)	$E(\text{GPa})$	200
Poisson's ratio $\nu$	$\nu$	0.28
Density $D$ ( $\text{kg}\cdot\text{m}^{-3}$ )	$D(\text{kg}\cdot\text{m}^{-3})$	7800
Specific heat $c$ ( $\text{J}\cdot\text{kg}^{-1}\cdot\text{C}^{-1}$ )	$\sigma_{y0}(\text{MPa})$	1134
Fraction of plastic work converted into heat $\eta$	0.9	—
$\sigma_{y0}(\text{MPa})$	324	—
$A(\text{MPa})$	114	—
$n$	0.42	—
$\dot{\varepsilon}_s^p(\text{s}^{-1})$	0.001	—
$\alpha(\text{MPa})$	4.52	—
$\beta(\text{MPa})$	0.65	—
$\sigma_{cr}(\text{GPa})$	1.5	—
$\dot{\varepsilon}_u^p(\text{s}^{-1})$	200	—
$B(\text{MPa})$	22	—
$T_R(\text{C})$	25	—
$T_m(\text{C})$	652	—
$T_d(\text{C})$	186.7	—
$b$	10.00	—
$m$	0.05	—

advantages in accurately describing such response behaviors of materials (particularly AA6061) have been demonstrated well [55–57]. Therefore, the MW material model was sourced to enable the high-accuracy reproduction of material response behaviors of AA6061 microparticles and substrates, as expressed in the following equation:

$$\sigma = \left\{ [\sigma_{y0} + A(\varepsilon^p)^n] + (\alpha\varepsilon^p + \beta) \left[ 1 - \frac{\sigma_{y0} + A(\varepsilon^p)^n}{\sigma_{cr}} \right] \ln \left( \frac{\dot{\varepsilon}^p}{\dot{\varepsilon}_s^p} \right) + B \ln \left( \frac{\dot{\varepsilon}^p}{\dot{\varepsilon}_u^p} \right) \right\} \left\{ \frac{\text{sigmoid} \left( -\frac{T-T_a}{T_m-T_a} b \right)}{\text{sigmoid} \left( -\frac{T_R-T_a}{T_m-T_a} b \right)} \right\}^m \quad (1)$$

where  $\sigma$  denotes the flow stress as a function of effective plastic strain  $\varepsilon^p$ , plastic strain rate  $\dot{\varepsilon}^p$ , and temperature  $T$ . The right-hand side of the equation can be divided into four terms:  $\sigma_I = \sigma_{y0} + A(\varepsilon^p)^n$ ,  $\sigma_{II} = (\alpha\varepsilon^p + \beta) \left[ 1 - \frac{\sigma_{y0} + A(\varepsilon^p)^n}{\sigma_{cr}} \right] \ln \left( \frac{\dot{\varepsilon}^p}{\dot{\varepsilon}_s^p} \right)$ ,  $\sigma_{III} = B \ln \left( \frac{\dot{\varepsilon}^p}{\dot{\varepsilon}_u^p} \right)$ , and  $f(T) = \left[ \frac{\text{sigmoid} \left( -\frac{T-T_a}{T_m-T_a} b \right)}{\text{sigmoid} \left( -\frac{T_R-T_a}{T_m-T_a} b \right)} \right]^m$ , representing different control mechanisms, in order of strain hardening, normal-range strain-rate hardening, ultra-high strain-rate hardening, and thermal softening/hardening.  $T_R$  and  $T_m$  are reference and melting temperatures, as well as  $\sigma_{y0}$ ,  $A$ ,  $n$ ,  $\alpha$ ,  $\beta$ ,  $\sigma_{cr}$ ,  $\dot{\varepsilon}_s^p$ ,  $\dot{\varepsilon}_u^p$ ,  $T_a$ ,  $b$ , and  $m$  are model parameters, which can be determined sequentially by flow stress-plastic strain, -temperature, and -strain rate curves. Failure occurs when materials undergo large plastic deformation, as represented by the plastic failure strain  $\varepsilon_f^p$  of 2 in the modeling. For more details, see Section 4.2 and Ref. [58]. The large-size SS410 particles did not suffer from visible plastic deformation because of their much higher strength and lower impact velocity than those of AA6061 microparticles; hence, their material response behaviors during in situ shot-peening-assisted CSAM can be described by the elastic-perfectly plastic material model. Using the material model further evidences the conclusion that large-size SS410 particles have almost no deformation (see Section 4.2 for more details). All parameters of AA6061 and SS410 used for material models are listed in Table 1.

Extreme deformation is often accompanied by high dislocation density and consequent grain refinement, where the average grain sizes are constantly decreasing, accompanied by the misorientation accumulation between adjacent dislocation cells. The early stages generate dislocation cell structures that evolve into ultimate fine-grain structures;

**Table 2**

Model parameters for describing the AA6061 microstructure evolution and strengthening of microhardness.

Parameters	
$\alpha^*$	0.0024
$\beta^*$	0.0054
$k_0$	3.22
$n_T$	67
$b_v(\text{m})$	$2.86 \times 10^{-10}$
$\dot{\gamma}_0(\text{s}^{-1})$	1
$M$	3.06
$f_0$	0.25
$f_\infty$	0.06
$\rho_c^{t=0}(\text{m}^{-2})$	$1.0 \times 10^{14}$
$\rho_w^{t=0}(\text{m}^{-2})$	$1.0 \times 10^{13}$
$\tilde{\gamma}$	3.2
$K$	44
$k_h$	0.25
$a$	0.25
$G(\text{GPa})$	26

this is the most widely accepted model of grain refinement triggered by large plastic deformation [59–63]. The model can be expressed by equations to enable coupling with the MW material model. The dislocation density consists of two components, i.e., the cell interior dislocation density ( $\rho_c$ ) and cell wall dislocation density ( $\rho_w$ ) divided by the statistical dislocation density  $\rho_{ws}$  and geometrically necessary dislocation density  $\rho_{wg}$ , whose evolutions can be captured by the following equations:

$$\dot{\rho}_c = \alpha^* \frac{1}{\sqrt{3}b_v} \sqrt{\rho_w} \dot{\gamma}_w - \beta^* \frac{6}{b_v d(1-f)^{1/3}} \dot{\gamma}_c - k_0 \left( \frac{\dot{\gamma}_c}{\dot{\gamma}_0} \right)^{-1/n_T} \rho_c \dot{\gamma}_c \quad (2)$$

$$\dot{\rho}_w = \beta^* \frac{\sqrt{3}(1-f)}{fb_v} \sqrt{\rho_w} \dot{\gamma}_c + \beta^* \frac{6(1-f)^{2/3}}{b_v df} \dot{\gamma}_c - k_0 \left( \frac{\dot{\gamma}_w}{\dot{\gamma}_0} \right)^{-1/n_T} \rho_w \dot{\gamma}_w \quad (3)$$

The terms on the right-hand side of the equations correspond to the different dislocation mechanisms. The 1st terms of Eqs. (2) and (3) denote the generation rates of cell interior/wall dislocations by activating Frank–Read sources at interfaces. The 2nd terms represent the relative transfer rates of dislocations from the cell interiors to walls and become part of the walls, and the 3rd terms account for the mutual annihilation rates of cell interior/wall dislocations causing dynamic recovery during deformation. Here,  $\alpha^*$ ,  $\beta^*$ , and  $k_0$  are the model parameters associated with each evolution rate,  $n_T$  is the temperature sensitivity exponent,  $b_v$  is the magnitude of the Burgers vector, and  $\dot{\gamma}_0$  is the reference resolved shear strain rate, respectively.  $\dot{\gamma}_c$  and  $\dot{\gamma}_w$  represent the resolved shear strain rates for cell interiors and walls, assumed to be equal as

$$\dot{\gamma}_c = \dot{\gamma}_w = M\dot{\varepsilon} \quad (4)$$

where  $\dot{\varepsilon}$  refers to the effective strain rate, and  $M$  represents the Taylor factor. Moreover,  $f$  is the volume ratio of dislocation walls, calculated as

$$f = f_\infty + (f_0 - f_\infty) e^{-\tilde{\gamma}} \quad (5)$$

where  $f_0$  and  $f_\infty$  are the initial and saturation volume ratios of dislocation walls, as well as  $\tilde{\gamma}$  is a parameter that nondimensionalizes the resolved shear strain  $\gamma$  ( $\gamma = Me$ ,  $e$  is the effective strain) for describing the evolution rate  $f$ . Hence, the total dislocation density  $\rho_{tot}$  can be evaluated using the following mixing rule as

$$\rho_{tot} = f(\rho_{ws} + \rho_{wg}) + (1-f)\rho_c \quad (6)$$

Correspondingly, the average dislocation cell size  $d$  can be given as

$$d = \frac{K}{\sqrt{\rho_{tot}}} \quad (7)$$

where  $K$  is the model parameter related to strains. Notably,  $d$  reproduced at large plastic deformation can indicate the average sub-grain size appropriately and be compared with the experimental results [59–62].

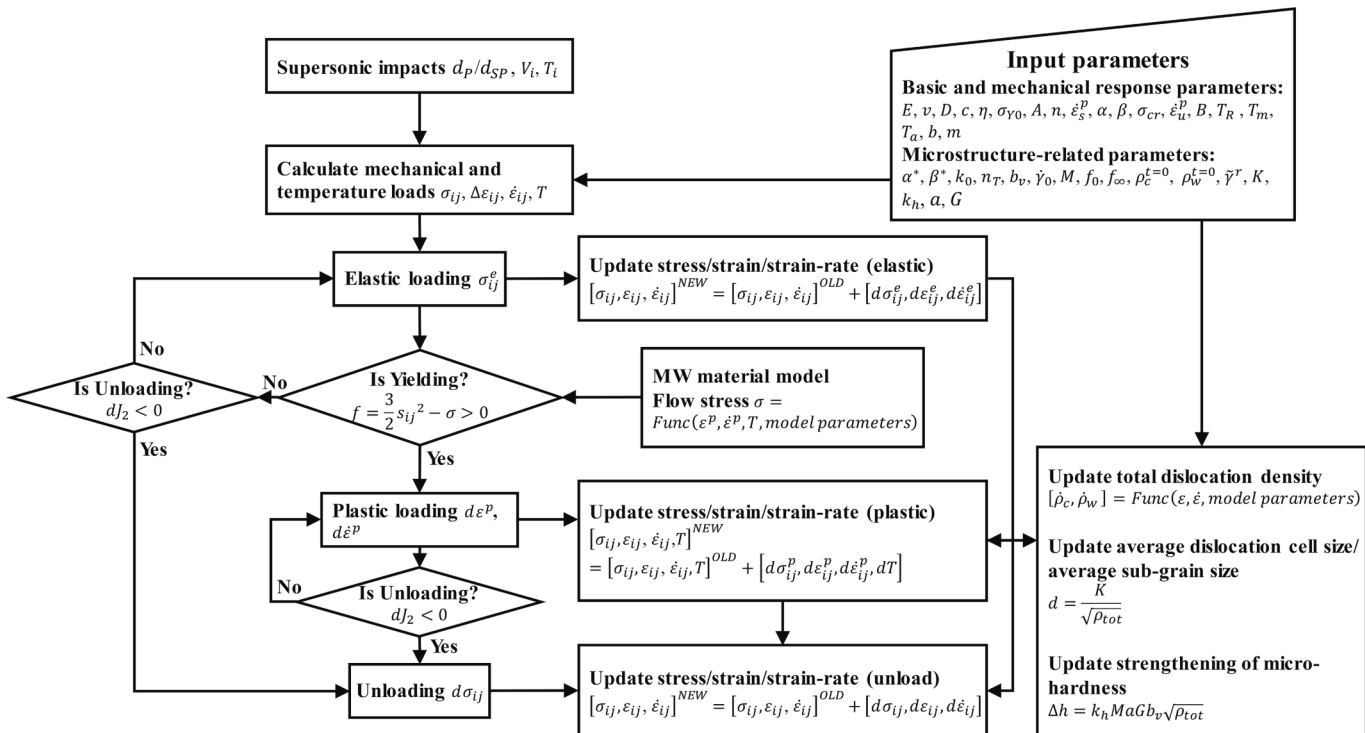


**Fig. 2.** Material modeling strategy implemented via sub-routine development to simulate the material response behaviors during conventional and in situ shot-peening-assisted CSAMs.

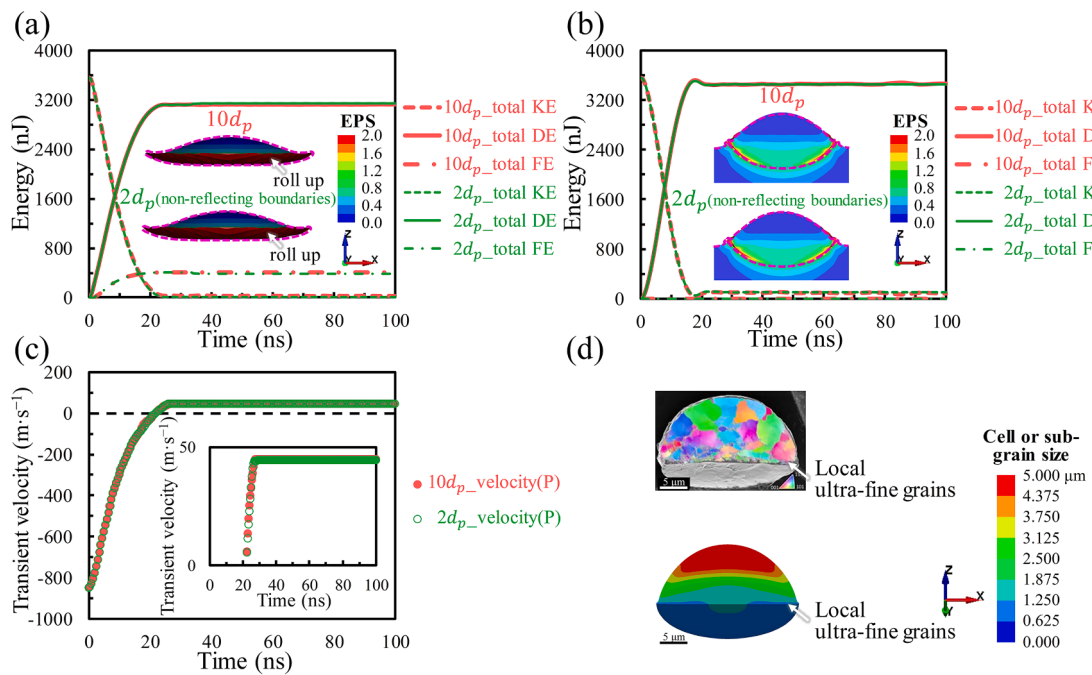


**Fig. 3.** Comparison of the overall energy conversions, overall deformations, and transient particle velocities using substrate sizes of  $10 d_p$  and  $2 d_p$ (non-reflecting boundaries) for (a,c) AA6061/sapphire and (b) AA6061/AA6061 impact systems at a  $d_p$  of  $19.1 \mu\text{m}$  of and  $V_i$  of  $850 \text{ m}\cdot\text{s}^{-1}$ . (d) Actual and model-reproduced grain refinement phenomena for AA6061/sapphire at a  $d_p$  of  $20.9 \mu\text{m}$  and  $V_i$  of  $530 \text{ m}\cdot\text{s}^{-1}$ . KE, DE, and FE refer to the kinetic, deformation, and friction energies, respectively. Actual deformation profiles for both impact systems are marked with purple dotted outlines.

Furthermore, the microhardness dependence on the refined microstructure regarding dislocation density can be expressed by Bailey–Hirsch (or Taylor) relationship [61,64] as

$$\Delta h = k_h M a G b_v \sqrt{\rho_{tot}} \quad (8)$$

where  $\Delta h$  denotes the strengthening of microhardness, as well as  $k_h$  is the slope of the Hall–Petch plot,  $a$  is the dislocation interaction factor, and  $G$  is the shear modulus, respectively. All model parameters used to describe the AA6061 microstructure evolution and strengthening of microhardness are listed in Table 2. Overall, the hybrid framework is schematized in Fig. 2 and implemented via sub-routine development to reproduce the material response behaviors during conventional and in situ shot-peening-assisted CSAMs, quantifying the process-microstructure-performance relationship.

#### 4. Results

##### 4.1. Conventional CSAM (basis & comparison object)

Adequate confirmation of model accuracy was required in advance of detailed discussion. The ability of the MW material model to accu-

rately describe the AA6061 material response behavior has been fully affirmed at a wide range of impact velocities ( $180$ – $1130 \text{ m}\cdot\text{s}^{-1}$ ) for both impact systems, AA6061/AA6061 and AA6061/sapphire, in our previous study [56]. Further, in this study, the reflection-free boundaries were designed to guarantee the high accuracy of simulations with more substantial computational cost savings. Fig. 3 compares the overall energy conversions, overall deformations, and transient particle velocities using a sufficiently large substrate size and a substrate size of  $2 d_p$  with non-reflecting boundaries for both impact systems at a  $d_p$  of  $19.1 \mu\text{m}$  of and impact velocity ( $V_i$ ) of  $850 \text{ m}\cdot\text{s}^{-1}$ . It is evident that the energy conversions and deformations using different substrate settings are identical for both impact systems (Fig. 3a and b); further, the results are in good agreement with those obtained by the experiments. Moreover, the rebound velocity of AA6061 microparticle can be accurately reproduced by using non-reflecting boundaries (Fig. 3c). Previous results showed that in the cases of non-reflecting boundaries, reducing the substrate size from  $10 d_p$  to  $2 d_p$  causes a slight increase in the rebound velocity because of interference of false waves. As a result, the effectiveness of the non-reflecting boundaries is demonstrated. In addition to the deformation behavior, the grain refinement phenomena were emphasized in this study. Therefore, the model accuracy in predicting grain refinement was further confirmed, as shown in Fig. 3d. Actual grain

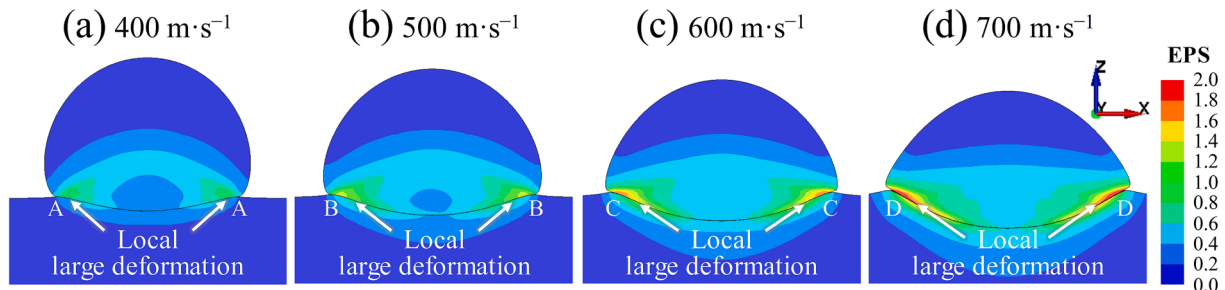


**Fig. 4.** Overall deformations of AA6061 microparticles ( $d_p = 34 \mu\text{m}$ ) after supersonic impacts at (a) 400, (b) 500, (c) 600, and (d) 700  $\text{m}\cdot\text{s}^{-1}$  without in situ shot-peening.

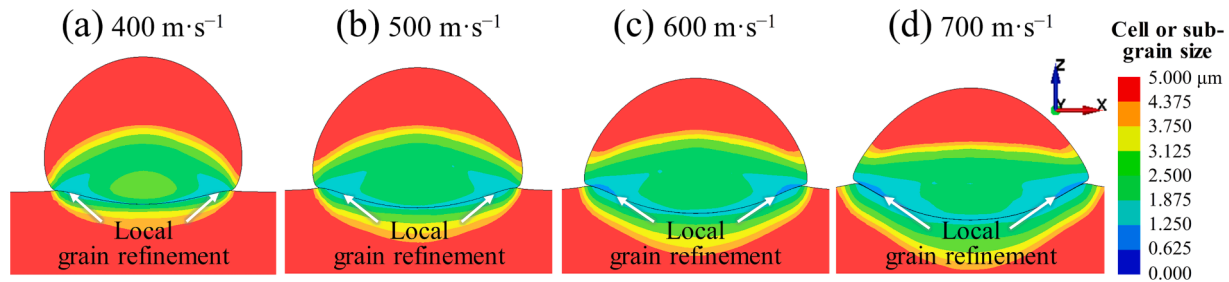


**Fig. 5.** Grain refinements of AA6061 microparticles ( $d_p = 34 \mu\text{m}$ ) after supersonic impacts at (a) 400, (b) 500, (c) 600, and (d)  $700 \text{ m}\cdot\text{s}^{-1}$  without in situ shot-peening.

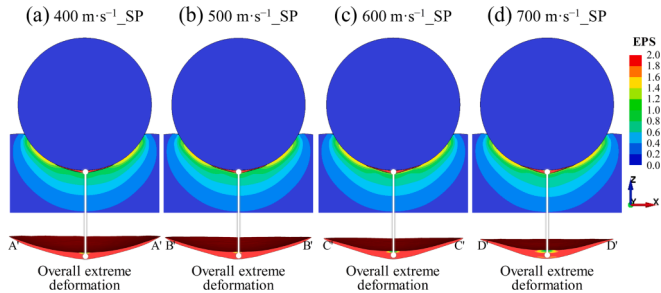


**Fig. 6.** Overall deformations of AA6061 microparticles ( $d_p = 34 \mu\text{m}$ ) after supersonic impacts at (a) 400, (b) 500, (c) 600, and (d)  $700 \text{ m}\cdot\text{s}^{-1}$  with in situ shot-peening.

refinement is increasingly significant from the top to the interface, and local ultra-fine grains exist near the interface. Both phenomena can be reproduced correctly, demonstrating the model accuracy in predicting grain refinement.

Before studying in situ shot-peening-assisted CSAM, the effects of AA6061 microparticle self-impact in conventional CSAM are understood explicitly. Fig. 4 displays the overall deformations with detailed effective plastic strain (EPS) distributions of AA6061 microparticles ( $d_p = 34 \mu\text{m}$ ) at different impact velocities. The particle deformation becomes more obvious as  $V_i$  increases, whereas the deformation pattern does not alter. Self-impact of AA6061 microparticles exhibits prominent non-uniform deformation characteristics. The top regions of AA6061 microparticles are almost undeformed, with increasingly significant deformation toward the interface. Large plastic deformation occurs mainly near the interface, especially at the edge of the interface. The uneven interfacial deformation coincides with the non-uniformity of interfacial bonding, supporting the decisive role of deformation in bonding [41,65,66].

Correspondingly, the grain refinements of AA6061 microparticles ( $d_p = 34 \mu\text{m}$ ) at different impact velocities are shown in Fig. 5. With increasing  $V_i$ , grain refinement becomes obvious, but the distribution pattern remains unchanged. There are distinct non-uniformities in grain refinement. Overall, grain refinement occurs near the interface and not at the top. Further observation near the interface indicates that fine grains mainly occur near the interface edge rather than the center. Moreover, the fine grain region at the interface edge increases with the increase in  $V_i$ . Both uneven interfacial deformation and grain refinement coincide with the non-uniformity of interfacial bonding, which further suggests deformation-induced oxide film rupture and dynamic recrystallization as the underlying cause of bonding [55,67]. The above results lay the foundation for illustrating the critical role of in situ shot-peening subsequently.

#### 4.2. Influence of in situ shot-peening on extreme deformation

The role of in situ shot-peening particles in the deformations of

deposited microparticles has not been clearly elucidated. To clarify this aspect, we performed a series of simulations to visualize the deformation effects of large-size SS410 particles on AA6061 microparticles, as shown in Fig. 6. The simulation model corresponding to Fig. 6b was established in accordance with the experiment, in which AA6061 microparticle and large-size SS410 particle sequentially impacted at the same location with impact velocities of  $500 \text{ m}\cdot\text{s}^{-1}$  and  $285 \text{ m}\cdot\text{s}^{-1}$ . The simulation models corresponding to Fig. 6a, c, and d assumed different impact velocities for AA6061 microparticles based on Fig. 6b to allow for a detailed discussion from two perspectives: (1) impact velocity and (2) in situ shot-peening. As we all know, during conventional CSAM, the  $V_i$  of microparticles is a critical process parameter that affects their deformation (Fig. 4). Nevertheless, the impact of in situ shot-peening particles rather than microparticles themselves dominates the deformation during in situ shot-peening-assisted CSAM. Regardless of the  $V_i$  of AA6061 microparticles, they underwent overall extreme deformation with the assistance of large-size SS410 particles (Fig. 6). Large-size SS410 particles were deformed negligibly during the process. As a minor note, local EPS at the top center slightly reduces as  $V_i$  increases. The possible reason is that the AA6061 microparticle becomes flatter (lower height) at higher  $V_i$ , leaving more limited deformation space for impact by large-size SS410 particles (identical ultimate deformation curvatures). In reality, the impact position of large-size SS410 particles with AA6061 microparticles deviates, and this local EPS reduction at the top center can be avoided. This is not detailed here.

To better understand the in situ shot-peening effects, the simulations presented in Fig. 4 and Fig. 6 are directly compared and shown in Fig. 7. First, the overall particle deformations are focused (Fig. 7a–d). FR is short for flattening ratio ( $\text{FR} = w/h$ ), where  $w$  and  $h$  are the width and height, respectively, of a deposited AA6061 microparticle. Increasing  $V_i$  facilitates deformation for the self-impact of AA6061 microparticles. FR increases gradually from 1.35 to 1.78 as  $V_i$  increases. Although the  $V_i$  of large-size SS410 particles ( $285 \text{ m}\cdot\text{s}^{-1}$ ) is only half those of AA6061 microparticles, the presence of these large particles dramatically improves the overall deformations of AA6061 microparticles (FR rises to approximately 20). In other words, the  $V_i$  of AA6061 microparticles themselves is no longer the dominant factor in deformation with the assistance of large-size SS410 particles. The impact of large-size SS410 particles enables overall extreme deformations of AA6061 microparticles. Incidentally, from the point of view of fundamental physical understanding, the overall true strain can be estimated by the following equation:

$$\varepsilon_{true} = \int_h^{d_p} \frac{dh}{h} = \ln\left(\frac{d_p}{h}\right) \quad (9)$$

which is more suitable for comparison with modeling [68]. The  $\varepsilon_{true}$  values after the impact of large-size SS410 particles at different impact velocities are 1.89, 1.78, 1.70, and 1.63, respectively, all close to 2, signifying the rationality of  $\varepsilon_f^p$  setting in Section 3.2.

Second, more attention is paid to the contact area variations at interfaces (Fig. 7e). As  $V_i$  increases, the final contact area (light blue

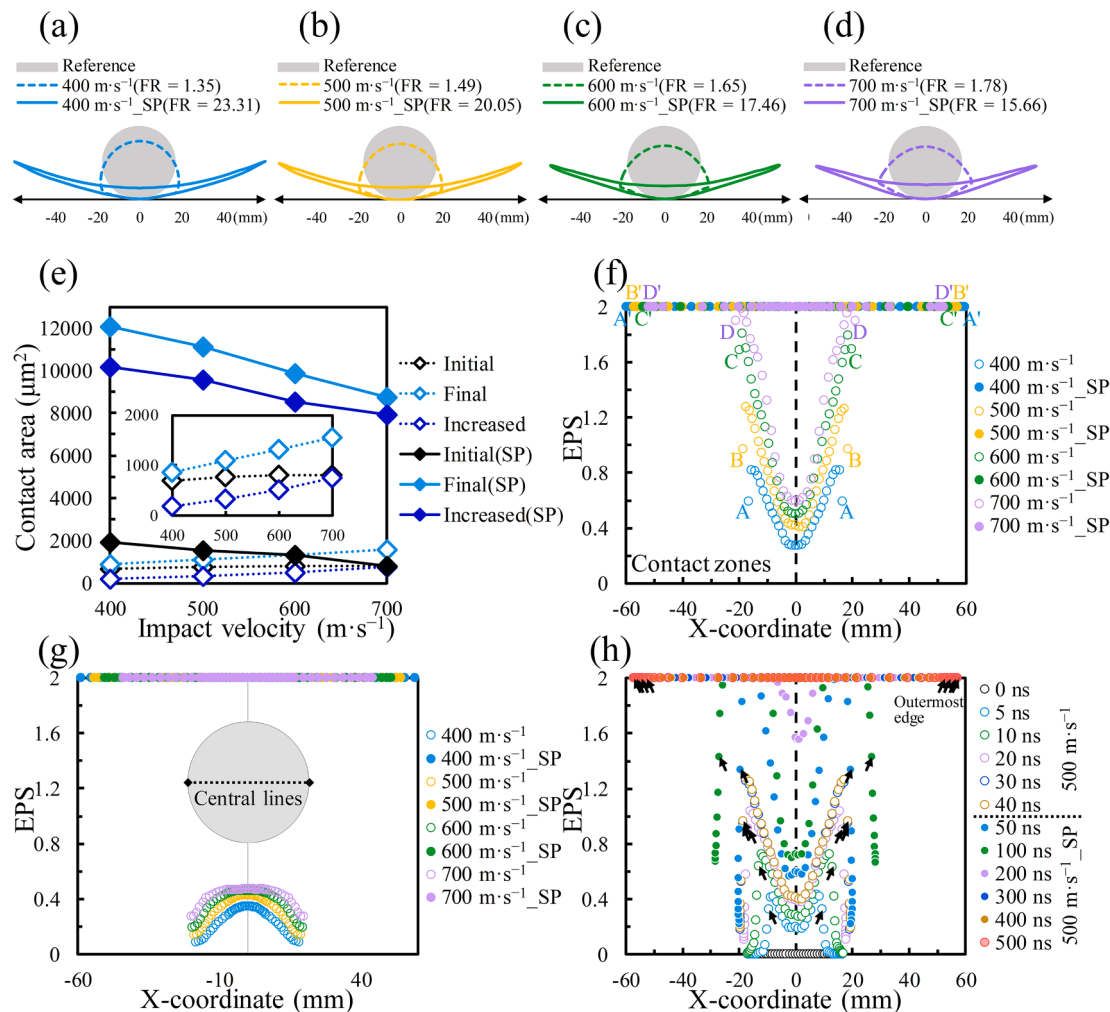


**Fig. 7.** Comparison of the (a–d) overall deformations, (e) contact areas, EPSs at (f) contact zones and along (g) central lines after supersonic impacts at 400, 500, 600, and 700 m·s<sup>-1</sup> without and with in situ shot-peening. (h) EPS evolution at the contact zone at a  $V_i$  of 500 m·s<sup>-1</sup> without and with in situ shot-peening. These data were extracted from the simulations in Fig. 4 and Fig. 6.

dotted line with rhombuses) caused by the impact of AA6061 microparticle itself increases while the corresponding initial contact area (black dotted line with rhombuses) decreases. As a result, the increased contact area (dark blue dotted line with rhombuses), symbolizing the bare-leakage metal direct contact area, increases with the increase in  $V_i$ , which is believed to be why  $V_i$  favors interfacial bonding. The increased contact areas (dark blue solid line with rhombuses) after the impact of large-size SS410 particles are much larger, more than 10 times, demonstrating the remarkable contribution of in situ shot-peening to deformation and interfacial bonding. Further, the local EPSs at contact zones and along central lines without and with in situ shot-peening are detailed (Fig. 7f and g). The local EPS distributions highlight the non-uniform deformation of AA6061 microparticles without in situ shot-peening and their overall extreme deformation with in situ shot-peening. Moreover, it is clarified that increasing  $V_i$  mainly contributes to interfacial deformation and enhances interfacial non-uniformity. In particular, the EPS evolution at the contact zone in the experiment-based simulation is presented (Fig. 7h). It is identified how the deformation of the AA6061 microparticle transforms from non-uniform to uniform and the outward shift of the outermost edge.

As mentioned above, the  $V_i$  of large-size SS410 particles (285 m·s<sup>-1</sup>) is only half those of AA6061 microparticles, but their influence on deformation is indeed dominant. The primary reason is that the large-size SS410 particle brings substantial kinetic energy (KE) notwithstanding the low  $V_i$ . To determine this, a detailed comparative analysis

of energy conversions with and without in situ shot-peening was undertaken, as shown in Fig. 8. During the self-impact of AA6061 microparticles (Fig. 8a), the total KE increases with the increase in  $V_i$  and is converted mostly into total deformation energy (DE), with slight recovery through elastic deformation and dissipated mostly through plastic deformation, causing microstructural evolution and temperature rise, etc. The total friction energy (FE) is close to zero.

Comparison of Fig. 8a and b indicates that within the impact of large-size SS410 particles, the total KE increases by two orders of magnitude and is partially converted into total FE in addition to total DE. The total FE originates from the large-size SS410 particle rubbing against the AA6061 microparticle and substrate, fueling interfacial bonding. The individual KEs and DEs were further detailed. The individual DEs of both AA6061 microparticle and substrate gradually increase with  $V_i$  (Fig. 8c). Nonetheless, these DEs are very, very small compared to the individual KEs of large-size SS410 particles (Fig. 8d). After the impact of large-size SS410 particles, the individual DEs of AA6061 microparticles reach  $\sim 3 \times 10^4$  nJ and no longer continue to increase; that is, they are independent of  $V_i$ . In short,  $\sim 3 \times 10^4$  nJ is speculated to be the limiting DE corresponding to the overall extreme deformation of individual AA6061 microparticles.

The simulation accuracy has been well-validated earlier. Here, we further validate the simulation accuracy while identifying the deformation differences between conventional and in situ shot-peening-assisted CSAM. First, the cross-sectional microstructures in Fig. 9a and

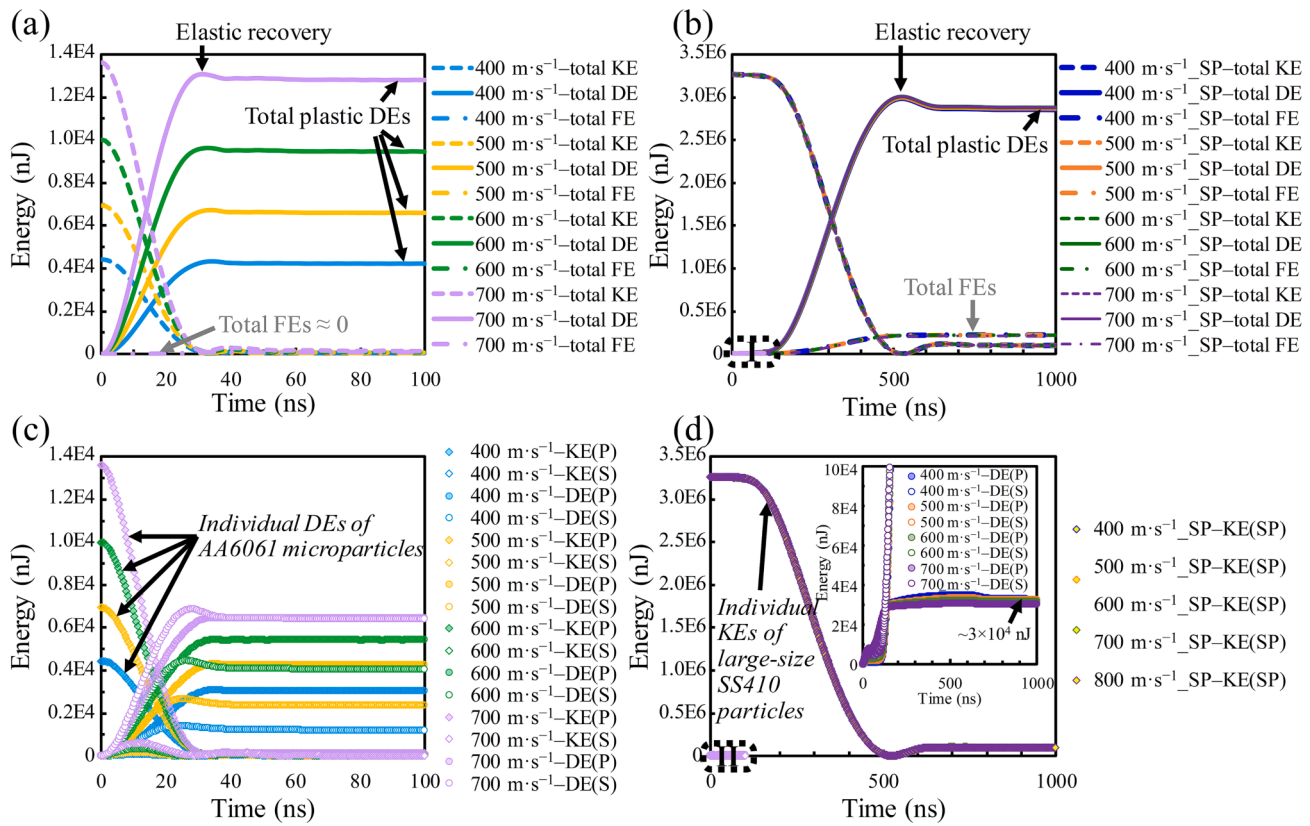


**Fig. 8.** (a,b) Overall energy conversions, (c,d) individual KEs and DEs of AA6061 microparticles ( $d_p = 34 \mu\text{m}$ ) after supersonic impacts at 400, 500, 600, and 700  $\text{m}\cdot\text{s}^{-1}$  without and with in situ shot-peening. Fig. 8a and c are enlargements of regions I and II of Fig. 8b and d, respectively. These data were extracted from the simulations in Fig. 4 and Fig. 6. KE, DE, and FE stand for kinetic, deformation, and friction energies, respectively. (P), (S), and (SP) denote the microparticle, substrate, and in situ shot-peening particles, respectively.

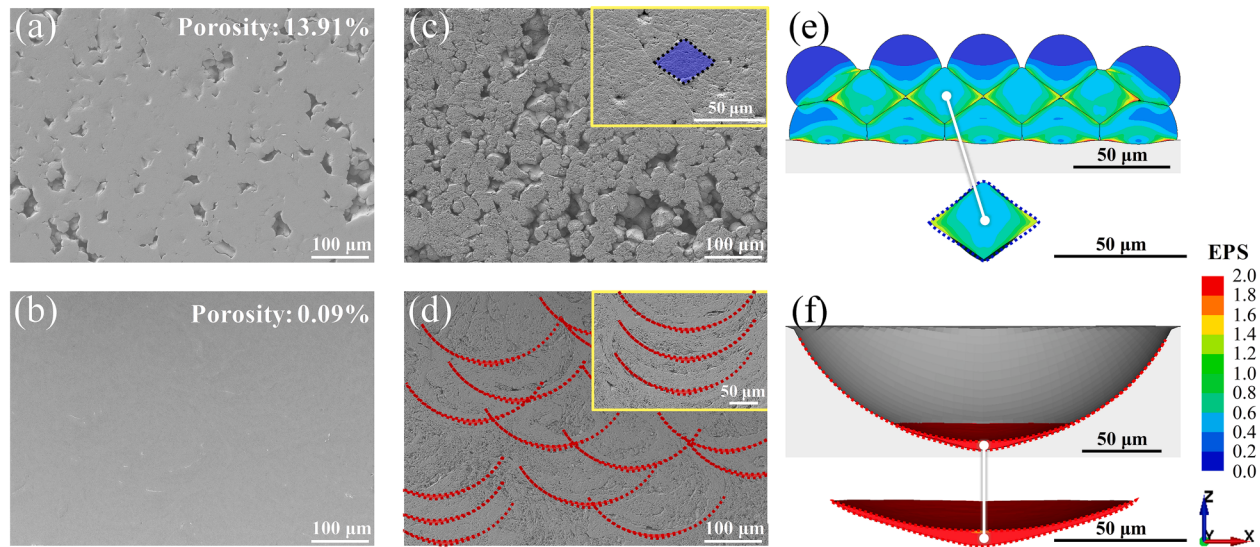


**Fig. 9.** Actual deformations of cold-spray additively manufactured AA6061 deposits at a  $V_i = 500 \text{ m}\cdot\text{s}^{-1}$  for AA6061 microparticles and  $285 \text{ m}\cdot\text{s}^{-1}$  for in situ shot-peening particles accounting for (a,c) 0 vol% and (b,d) 70 vol%, compared with those simulated (e) without and (f) with adequate in situ shot-peening. The simulated deformation profiles are marked as dotted outlines.

b indicate that sufficient deformation favors void/crack closure accompanied by a distinct decrease in porosity. That is, the key to highly dense deposits is the overall extreme deformation of AA6061 microparticles. Further etching was performed to expose the interparticle interfaces (Fig. 9c and d). The particle deformation profiles after conventional CSAM appear polygonal, and some are diamond-shaped,

reproduced correctly by the multi-particle impact simulation (Fig. 9e). This profile feature originates from the multi-interface deformation caused by interparticle collisions. In contrast, the deformation profiles of AA6061 microparticles after in situ shot-peening-assisted CSAM are clearly crescent-shaped. It correlates with the large-size SS410 particles, identified by comparing simulated deformation profile with actual ones

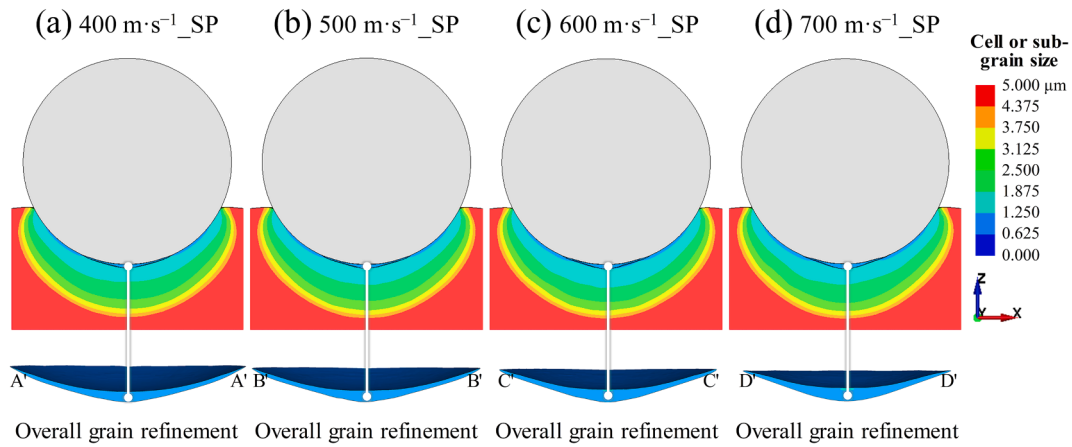


**Fig. 10.** Grain refinements of AA6061 microparticles ( $d_p = 34 \mu\text{m}$ ) after supersonic impacts at (a) 400, (b) 500, (c) 600, and (d) 700  $\text{m}\cdot\text{s}^{-1}$  with in situ shot-peening.

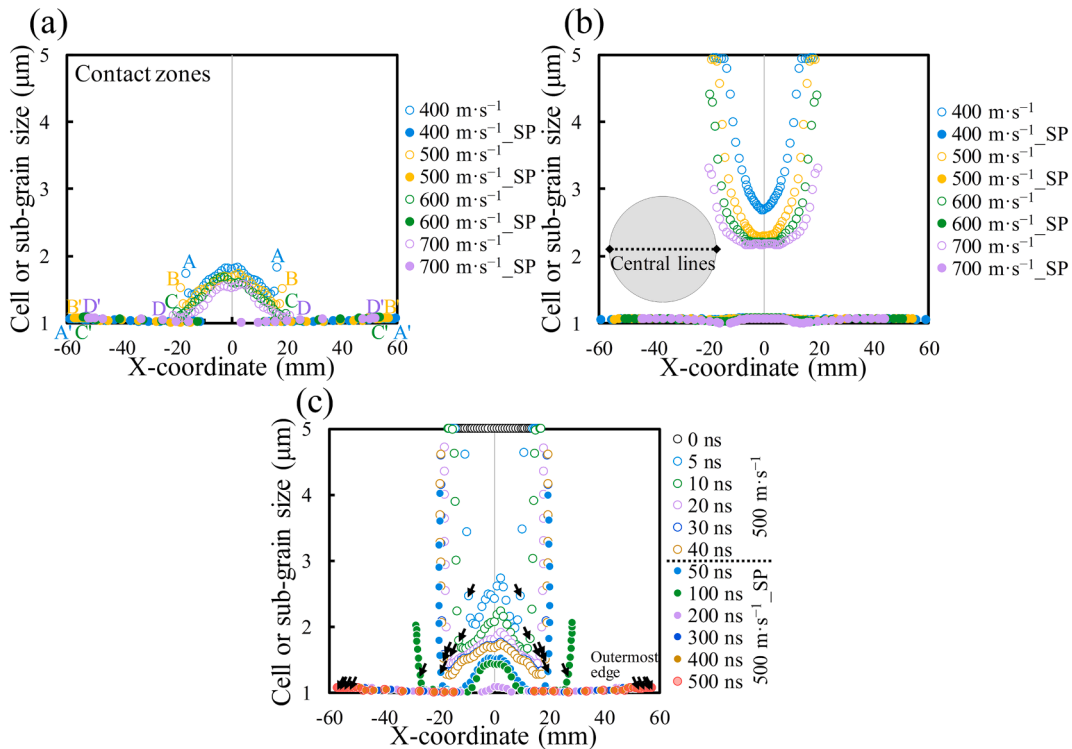


**Fig. 11.** Comparison of the cell or sub-grain sizes at (a) contact zones and along (b) central lines after supersonic impacts at 400, 500, 600, and 700  $\text{m}\cdot\text{s}^{-1}$  without and with in situ shot-peening. (c) cell or sub-grain size evolution at the contact zone at a  $V_i$  of 500  $\text{m}\cdot\text{s}^{-1}$  without and with in situ shot-peening. These data were extracted from the simulations in Fig. 5 and Fig. 10.

(Fig. 9d and f). Fig. 9 further evidences the validity of simulations and emphasizes the decisive role of large-size SS410 particles for the overall extreme deformation of AA6061 microparticles and the densification of the corresponding deposit.

#### 4.3. Influence of in situ shot-peening on grain refinement and mechanical performance

Large plastic deformation is inextricably linked to microstructural evolution. In Section 4.1, it is specified that the particle self-impact causes local large deformation and thus leads to non-uniform grain refinement. More intense deformation occurs with in situ shot-peening. However, the role of in situ shot-peening in grain refinement and the correlation with deformation are not well-understood. To illustrate this point fully, the grain refinements corresponding to Fig. 6 are reproduced

in Fig. 10. Fig. 10 displays the grain refinements of AA6061 microparticles after supersonic impacts at 400  $\text{m}\cdot\text{s}^{-1}$ , 500  $\text{m}\cdot\text{s}^{-1}$ , 600  $\text{m}\cdot\text{s}^{-1}$ , and 700  $\text{m}\cdot\text{s}^{-1}$  with in situ shot-peening. It is evident that the AA6061 microparticles exhibit overall grain refinement upon the impact of large-size SS410 particles. Moreover, uniform ultra-fine grains are implied as the result of overall extreme deformation. It effectively associates deformation with microstructure evolution. With in situ shot-peening, the grain refinement is almost unaffected by the  $V_i$  of AA6061 microparticles. It indicates the dominance of large-size SS410 particles for grain refinement. Consequently, overall grain refinement is another key role of in situ shot-peening.

To better understand the role of in situ shot-peening on grain refinement, simulations reproduced in Fig. 5 and Fig. 10 are directly compared and presented in Fig. 11. First, the local cell or sub-grain size distributions at contact zones and along central lines without and with in

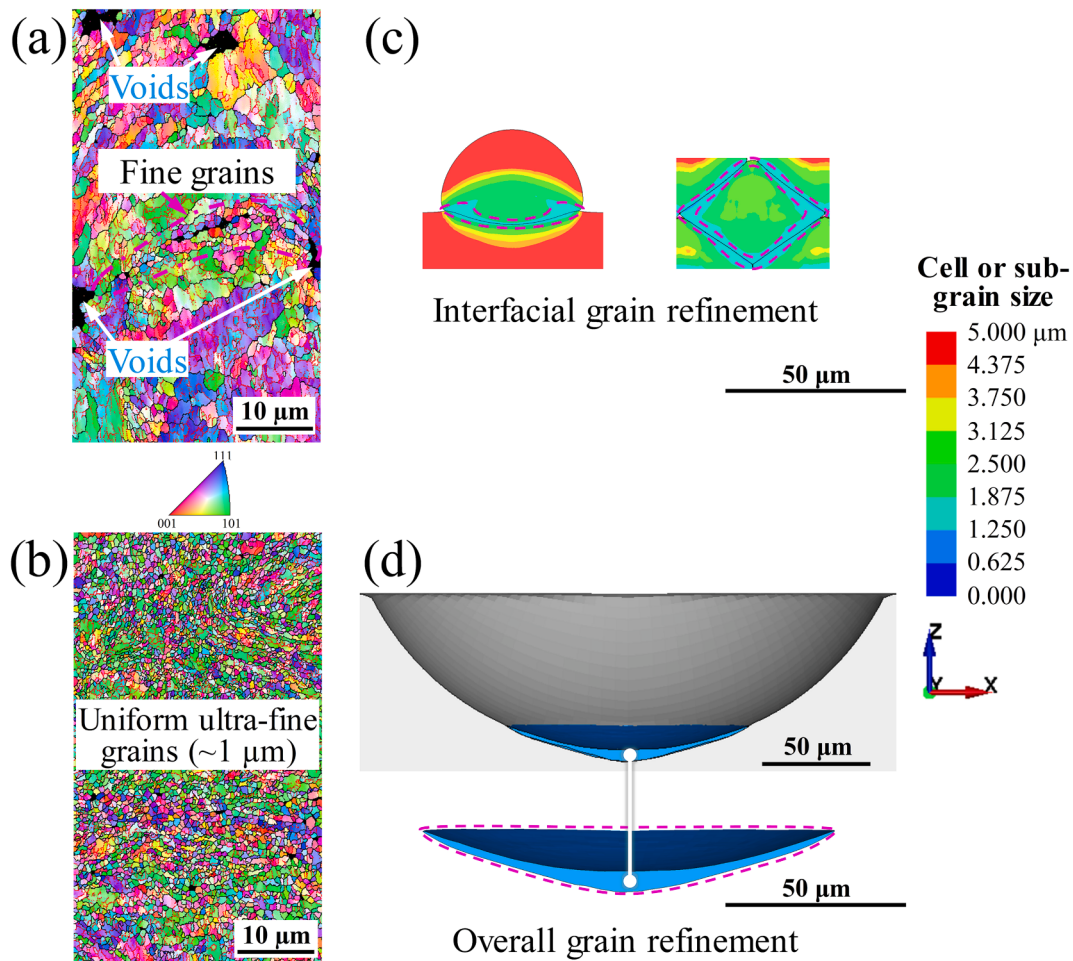


**Fig. 12.** Actual grain size distribution of cold-spray additively manufactured AA6061 deposits at a  $V_i$  of  $500 \text{ m}\cdot\text{s}^{-1}$  for AA6061 microparticles and  $285 \text{ m}\cdot\text{s}^{-1}$  for in situ shot-peening particles accounting for (a) 0 vol% and (b) 70 vol%, compared with those simulated (c) without and (d) with adequate in situ shot-peening. High-angle ( $>15^\circ$ ) and low-angle ( $5^\circ$ – $15^\circ$ ) grain boundaries are marked with black and red lines, respectively, in Fig. 12a and b.

situ shot-peening are detailed in Fig. 11a and b. It highlights the non-uniformity of grain refinement in particle self-impact. Unlike deformation, the non-uniformity is more prominent along central lines, depending on  $V_i$ . The model-reproduced smaller cells or sub-grains at the interface are derived from particle self-impact, mainly causing interface deformation. Meanwhile, the overall grain refinement by in situ shot-peening is underscored. Both the interface and interior of

AA6061 microparticles exhibit ultra-fine cells or sub-grains ( $\approx 1 \mu\text{m}$ ). Furthermore, the cell or sub-grain size evolution at the contact zone in the experiment-based simulation is shown explicitly (Fig. 11c), signifying the evolution from non-uniform to uniform ultra-fine grains. Grain refinement starts at the interface edge and then progresses to the interface center. The size obtained by refinement gradually decreases as the deformation proceeds. After particle self-impact, the cell or sub-grains at the interface edge are the smallest but exceed  $1 \mu\text{m}$  ( $\leq 40 \text{ ns}$ ). They are all as small as  $1 \mu\text{m}$  in the whole AA6061 microparticle with in situ shot-peening.

The actual grain size distributions of conventional and in situ shot-peening-assisted CSAM deposits were characterized by EBSD, as shown in Fig. 12a and b. High-angle ( $>15^\circ$ ) and low-angle ( $5^\circ$ – $15^\circ$ ) grain boundaries are marked with black and red lines, respectively. The difference in size distribution is striking. Fine grains caused by grain refinement in the conventional CSAM deposit appear mainly near the interface. The grain size inside the AA6061 microparticles is obviously larger than that at the interface. Incidentally, voids inevitably exist due to insufficient deformation of AA6061 microparticles, detailed in Section 4.2. The interfacial grain refinement can be reproduced by the corresponding single- and multi-particle impact simulations (Fig. 12c), identifying the characteristics of particle self-impact. In contrast, uniform ultra-fine grains of  $\sim 1 \mu\text{m}$  are observed in the in situ shot-peening-assisted CSAM deposits. The simulation (Fig. 12d) is in high agreement with the experiment, and, clearly, the uniform ultra-fine grains are determined by the overall extreme deformation induced by the impact of

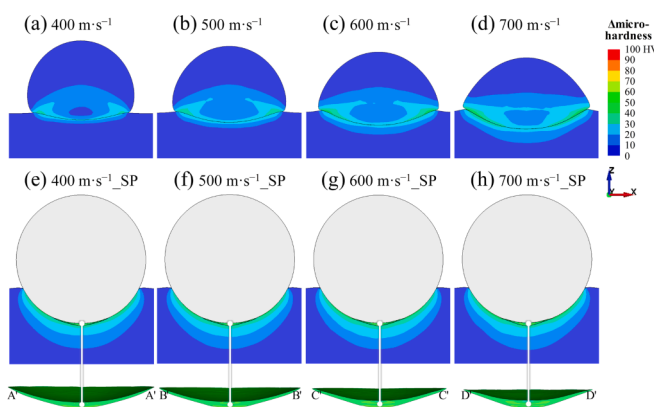


**Fig. 13.** Increases in microhardness of AA6061 microparticles ( $d_p = 34 \mu\text{m}$ ) after supersonic impacts at  $400$ ,  $500$ ,  $600$ , and  $700 \text{ m}\cdot\text{s}^{-1}$  (a–d) without and (e–h) with in situ shot-peening.

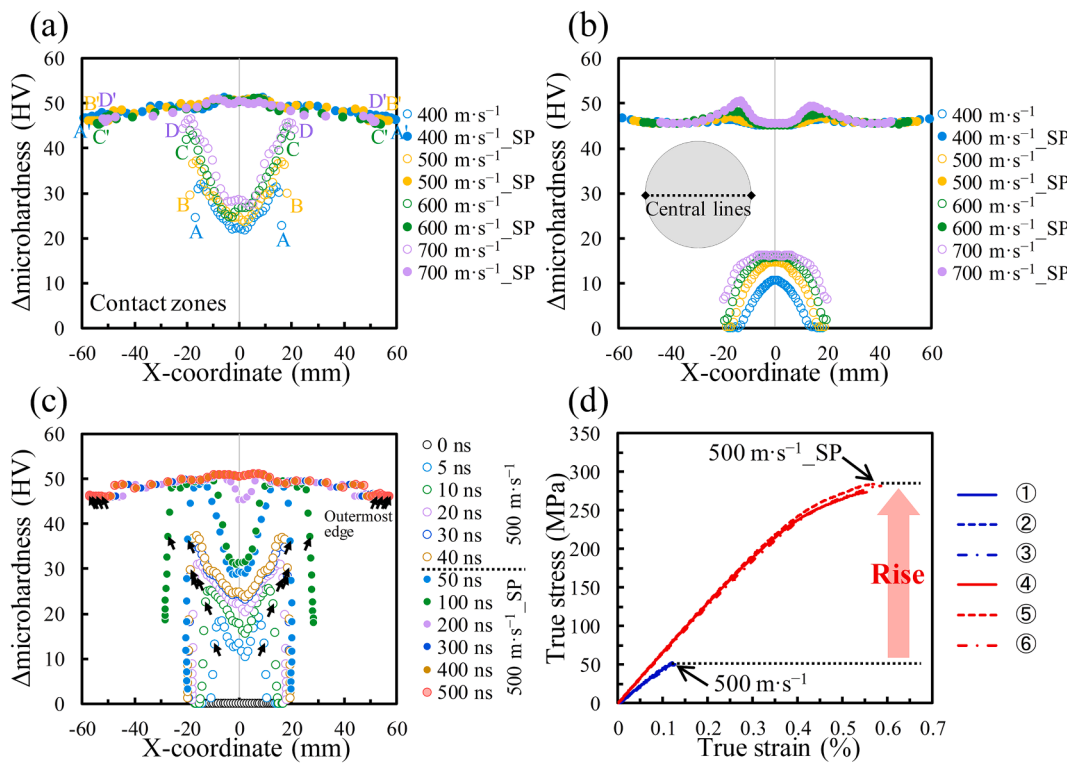


**Fig. 14.** Comparison of the increases in microhardness at (a) contact zones and along (b) central lines after supersonic impacts at 400, 500, 600, and 700  $\text{m}\cdot\text{s}^{-1}$  without and with in situ shot-peening. (c) Evolution of the microhardness increase at the contact zone at a  $V_i$  of 500  $\text{m}\cdot\text{s}^{-1}$  without and with in situ shot-peening and (d) the increase in strength of the corresponding cold-spray additively manufactured AA6061 deposits. These data were extracted from the simulations in Fig. 13.

large-size SS410 particles. Fig. 12 not only further solidifies the validity of simulations in reproducing grain refinement but also emphasizes the decisive role of large-size SS410 particles for uniform ultra-fine grains of AA6061 microparticles.

Microstructure evolution causes variations in mechanical performance. The microhardness depends on the refined microstructure regarding dislocation density, whose strengthening is estimated based on dislocation density and shown in Fig. 13. Fig. 13 compares the increases in microhardness of AA6061 microparticles without and with in situ shot-peening. The comparison indicates the deformation-microstructure-performance relationship. Similar to deformation and grain refinement, microhardness differs noticeably without and with in situ shot-peening. In the absence of in situ shot-peening, the microhardness increases of AA6061 microparticles are obviously unevenly distributed (Fig. 13a-d). It gradually increases from the top to the interface and reaches the maximum near the interface edge. However, when in situ shot-peening is used, the AA6061 microparticles exhibit overall significant increases in microhardness (Fig. 13e-h). As mentioned above, the AA6061 microparticles undergo overall extreme deformation (Fig. 6b) and overall grain refinement (Fig. 10b) during the

impact of large-size SS410 particles. Moreover, the in situ shot-peening-assisted CSAM deposit is highly dense (Fig. 9b). As a result, the simulated-reproduced average microhardness increase (=46.7 HV) is comparable to the experimental one (=41.5 HV<sub>0.05</sub>). Both of them indicate a significant increase in microhardness. Meanwhile, the consistency of microhardness increases further supports the validity of the simulation in correlating deformation, microstructure, and performance.

Similarly, to better understand the role of in situ shot-peening on microhardness, simulations reproduced in Fig. 13 are directly compared and displayed in Fig. 14a-c. The increases in microhardness at contact zones and along central lines are detailed in Fig. 14a and b. It highlights the non-uniformity of the particle self-impact microhardness and the significant increase in overall microhardness after the impact of large-size SS410 particles. Meanwhile, the evolution of the microhardness increases at the contact zone in the experiment-based simulation is presented in Fig. 14c to specify how the increases in microhardness shift from non-uniform to uniform. As a side note, the distribution similarity of  $\Delta$ microhardness to EPS (Fig. 11) also indirectly reflects the close correlation between deformation, microstructure, and performance.

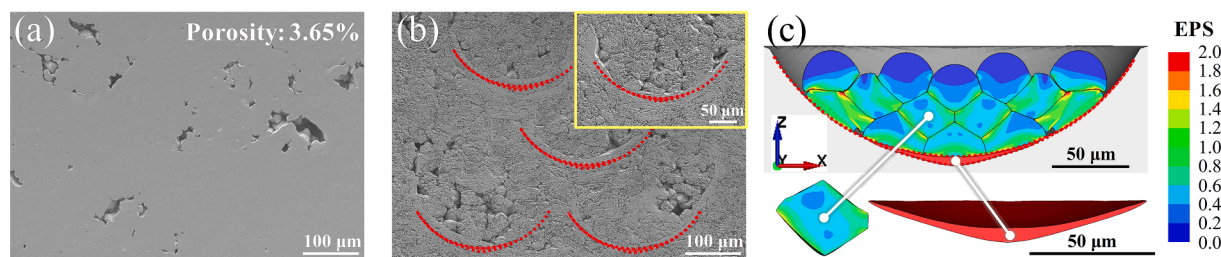


**Fig. 15.** Actual deformations of cold-spray additively manufactured AA6061 deposits at a  $V_i$  of 500  $\text{m}\cdot\text{s}^{-1}$  for AA6061 microparticles and 285  $\text{m}\cdot\text{s}^{-1}$  for in situ shot-peening particles accounting for (a,b) 30 vol%, compared with those simulated (c) with inadequate in situ shot-peening. The simulated deformation profiles are marked as dotted outlines.

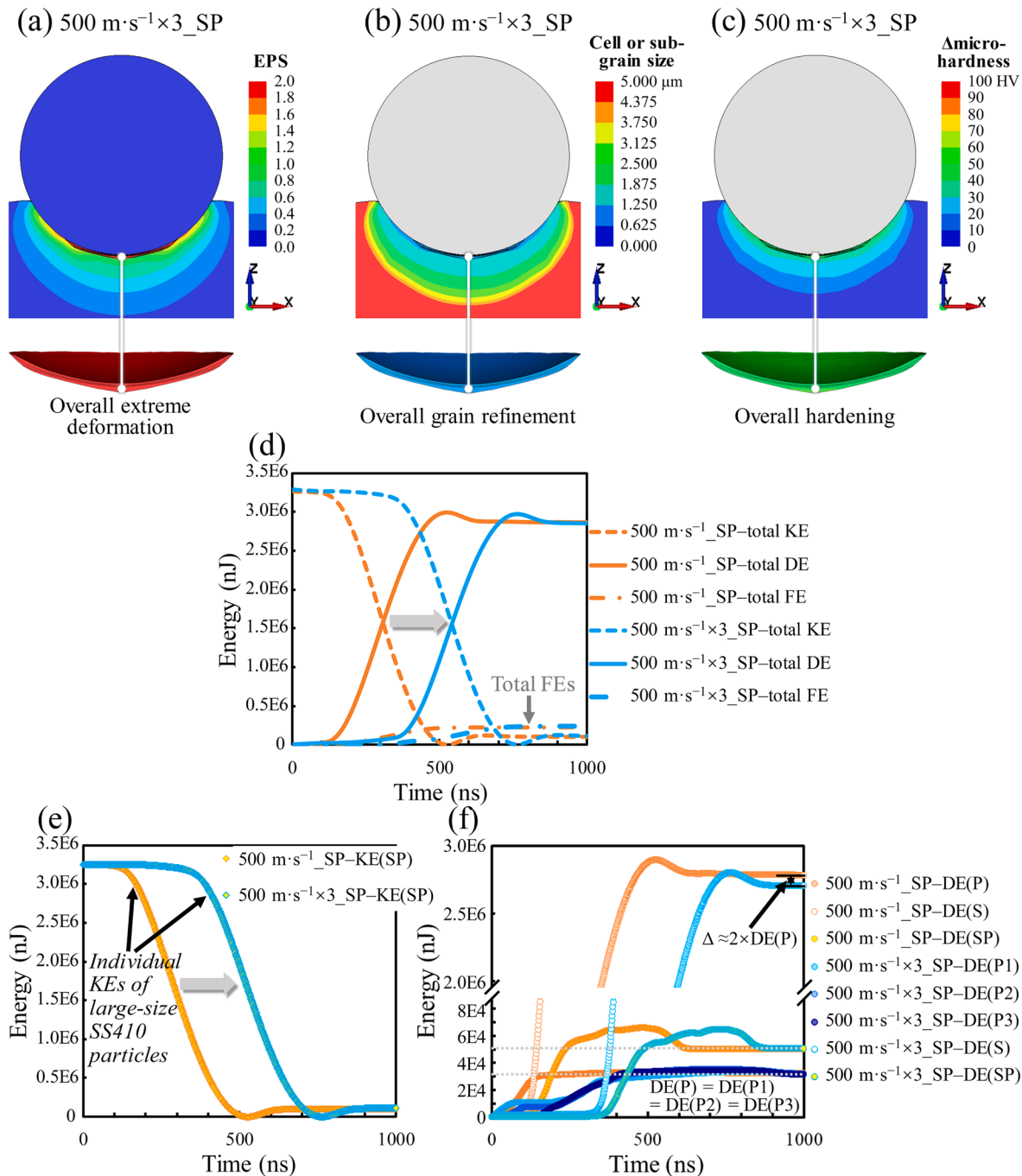


**Fig. 16.** (a) Overall deformation, (b) grain refinement, and (c) increase in microhardness of three AA6061 microparticles ( $d_p = 34 \mu\text{m}$ ) after supersonic impacts at  $500 \text{ m}\cdot\text{s}^{-1}$  with in situ shot-peening. Comparison of the (d) overall energy conversions and individual (e) KEs and (f) DEs after impacting one or three AA6061 microparticles with in situ shot-peening.

What is more, the actual tensile strengths of conventional and in situ shot-peening CSAM deposits are compared and displayed in Fig. 14d. The tensile strength climbs significantly owing to the impact of large-size SS410 particles. The prominent rise in tensile strength can be attributed to deformation-induced hardening and void/crack closure (Fig. 9a and b). The issue is complicated and left for future discussion.

## 5. Discussion

The key role of large-size SS410 particles, specifically in terms of extreme deformation, grain refinement, and strengthening of microhardness, has been elucidated and quantified above. The large-size

SS410 particles indeed bring enormous KE, but the DE(P) of individual particles is limited to  $3.26 \times 10^6 \text{ nJ}$ . Therefore, the mixing ratio of large-size SS410 particles to AA6061 microparticles is vitally important in actual in situ shot-peening-assisted CSAM. Fig. 15a and b shows the microstructure characteristics formed in the case of inadequate large-size SS410 particles. Obvious voids are present, but the porosity is lower than that of the corresponding conventional CSAM deposit (Fig. 9a). The etched cross-section indicates an alternating distribution of dense and multi-void zones in the deposit due to inadequate large-size SS410 particles. To make this clearer, our simulation reproduces this distribution feature, as shown in Fig. 15. It identifies that this distribution feature originates from the alternating overall extreme deformation

and local large deformation of AA6061 microparticles. Consequently, it is crucial to optimize the proportion of large-size SS410 particles.

The key to large-size SS410 particles is to generate the overall extreme deformation of AA6061 microparticles. As discussed above, the overall extreme deformation is accompanied by uniform ultra-fine grains and significant increases in microhardness. Notably, a single AA6061 microparticle as a whole suffers extreme deformation, and the dissipated DE reaches an extreme value ( $\sim 3 \times 10^4$  nJ in Fig. 8d). It is inferred that the proportion of large-size SS410 particles can be evaluated from the perspective of energy conversion. To verify this, the experiment-based simulation of depositing multiple AA6061 microparticles followed by in situ shot-peening was carried out, as shown in Fig. 16. Evidently, the impact of large-size SS410 particles is capable of causing the overall extreme deformations of multiple AA6061 microparticles (Fig. 16a). The AA6061 microparticles undergo overall extreme deformations, accompanied by overall grain refinements and hardenings (Fig. 16b and c).

Detailed energy information is presented by comparison with that after impacting one AA6061 microparticle with in situ shot-peening, as shown in Fig. 16d–f. In both systems, most of the total KE is converted into total DE, and only a small amount is converted into total FE (Fig. 16d). The noticeable difference is the rightward shift of the total KE, DE, and FE curves after multi-particle impact. This is reasonable because of the impact delay of the large-size SS410 particle (Fig. 16e). Further analysis of individual DEs of AA6061 microparticles and substrates is displayed in Fig. 16f. The DEs corresponding to the overall extreme deformations of multiple AA6061 microparticles are identical [i.e.,  $DE(P) = DE(P1) = DE(P2) = DE(P3) \approx 3.2 \times 10^4$  nJ]. The increase of DE dissipated by AA6061 microparticles arising from the increased amount corresponds to the decrease of DE in the AA6061 substrate. As a result, it is proposed that the minimum volume ratio of large-size SS410 particles  $\phi_{min}$  required to achieve fully dense AA6061 deposits with uniform ultra-fine grains can be estimated by the following equation:

$$\phi_{min} = \frac{1}{\eta_e \frac{DE(P+S)}{DE(P)} \frac{dp^3}{dsp^3} + 1} \quad (10)$$

where  $DE(P)$ ,  $DE(P + S)$ , and  $\eta_e$  represent the individual DE dissipated through the overall extreme deformation of a single AA6061 microparticle ( $\approx 3.2 \times 10^4$  nJ), the total DE dissipated by the AA6061 microparticle and substrate ( $\approx 2.8 \times 10^6$  nJ), and the deposition efficiency of AA6061 microparticles ( $\approx 40\%$ ), respectively. Therefore,  $\phi_{min}$  is estimated to be 69.60 vol%. Its high agreement with the actual one (70 vol%) further confirms the validity of simulations. More importantly, the microforging principle during in situ shot-peening-assisted CSAM is fully unraveled with the help of simulations, demonstrating the model's potential to guide process optimization.

## 6. Conclusions

Fully dense AA6061 deposits with uniform ultra-fine grains were fabricated by in situ shot-peening-assisted CSAM using low-cost renewable nitrogen gas and recyclable large-size SS410 particles. A multi-physics framework using dislocation dynamics was developed to identify its similarities and differences with conventional CSAM to unravel the microforging principle. Simulations were fully validated by comparing the model-reproduced and experimental deformations, grain refinement, microhardness increase, and volume ratio of large-size SS410 particles required to achieve full densification of the deposit. In situ shot-peening particles, despite having half the  $V_i$  of deposited microparticles, deliver two orders of magnitude higher KE. The enormous KE allows overall extreme deformation accompanied by overall grain refinement of the deposited microparticles, significantly improving microhardness and tensile strength. This work can provide scientific guidelines for high-quality and low-cost CSAM of high-strength Al alloys, contributing to SDGs and carbon neutrality. What is more, the

model in this study confers a direct correlation among process, microstructure, and performance, which is universal and can be well-expected as a tool for the optimal design of in situ shot-peening-assisted CSAM of various hard-to-deform metallic materials.

## Declaration of Competing Interest

The authors declare that they have no known competing financial interests or personal relationships that could have appeared to influence the work reported in this paper.

## Data availability

Data will be made available on request.

## Acknowledgments

This research was financially supported by the Japan Society for the Promotion of Science (Grants-in-Aid for Scientific Research: 20H02452 and 23K13577), Amada Foundation (AF-2022034-C2), as well as OU master project of Osaka University for promoting international collaboration research. The authors would like to appreciate the assistance of Mr. Masuo Ito in microstructure characterization. Prof. Luo and Prof. Li from Xi'an Jiaotong University appreciate the financial support from the National Natural Science Foundation of China (52375379) and Science Center for Gas Turbine Project (HT-P2022-B-IV-011-001).

## Appendix A. Supplementary data

Supplementary data to this article can be found online at <https://doi.org/10.1016/j.matdes.2023.112451>.

## References

- [1] M. Parsazadeh, S. Sharma, N. Dahotre, Towards the next generation of machine learning models in additive manufacturing: a review of process dependent material evolution, *Prog. Mater. Sci.* 135 (2023), 101102.
- [2] G. Liu, X. Zhang, X. Chen, Y. He, L. Cheng, M. Huo, J. Yin, F. Hao, S. Chen, P. Wang, S. Yi, Additive manufacturing of structural materials, *Mater. Sci. Eng. R-Rep.* 145 (2021), 100596.
- [3] I. Gibson, D. Rosen, B. Stucker, M. Khorasani, D. Rosen, B. Stucker, M. Khorasani, *Additive Manufacturing Technologies*, third ed., Springer Cham, Switzerland, 2021.
- [4] T. DebRoy, H.L. Wei, J.S. Zuback, T. Mukherjee, J.W. Elmer, J.O. Milewski, A. M. Beese, A.D. Wilson-Heid, A. De, W. Zhang, Additive manufacturing of metallic components-process, structure and properties, *Prog. Mater. Sci.* 92 (2018) 112–224.
- [5] S.M. Thompson, L. Bian, N. Shamsaei, A. Yadollahi, An overview of Direct Laser Deposition for additive manufacturing; Part I: transport phenomena, modeling and diagnostics, *Addit. Manuf.* 8 (2015) 36–62.
- [6] N. Shamsaei, A. Yadollahi, L. Bian, S.M. Thompson, An overview of Direct Laser Deposition for additive manufacturing; Part II: mechanical behavior, process parameter optimization and control, *Addit. Manuf.* 8 (2015) 12–35.
- [7] J.P. Oliveira, T.G. Santos, R.M. Miranda, Revisiting fundamental welding concepts to improve additive manufacturing: from theory to practice, *Prog. Mater. Sci.* 107 (2020), 100590.
- [8] D. Jafari, T.H. Vaneker, I. Gibson, Wire and arc additive manufacturing: opportunities and challenges to control the quality and accuracy of manufactured parts, *Mater. Des.* 202 (2021), 109471.
- [9] A. Palmquist, M. Jolic, E. Hryha, F.A. Shah, Complex geometry and integrated macro-porosity: clinical applications of electron beam melting to fabricate bespoke bone-anchored implants, *Acta Biomater.* 156 (2023) 125–145.
- [10] W.J. Sames, F.A. List, S. Pannala, R.R. Dehoff, S.S. Babu, The metallurgy and processing science of metal additive manufacturing, *Int. Mater. Rev.* 61 (2016) 315–360.
- [11] A. Mostafaei, R. Ghiasi, Aan, I.T. Ho, S. Strayer, K.C. Chang, N. Shamsaei, S. Shao, S. Paul, A.C. Yeh, S. Tin, A.C. To, Additive manufacturing of nickel-based superalloys: a state-of-the-art review on process-structure-defect-property relationship, *Prog. Mater. Sci.* 136 (2023), 101108.
- [12] T. Hauser, R.T. Reisch, P.P. Breese, Y. Nalam, K.S. Joshi, K. Bela, T. Kamps, J. Volpp, A.F. Kaplan, Oxidation in wire arc additive manufacturing of aluminium alloys, *Addit. Manuf.* 41 (2021), 101958.
- [13] S. Thapliyal, P. Agrawal, P. Agrawal, S.S. Nene, R.S. Mishra, B.A. McWilliams, K. C. Cho, Segregation engineering of grain boundaries of a metastable Fe-Mn-Co-Cr-Si high entropy alloy with laser-powder bed fusion additive manufacturing, *Acta Mater.* 219 (2021), 117271.

- [14] Y. Liu, J. Zhang, Q. Tan, Y. Yin, S. Liu, M. Li, M. Li, Q. Liu, Y. Zhou, T. Wu, F. Wang, Additive manufacturing of high strength copper alloy with heterogeneous grain structure through laser powder bed fusion, *Acta Mater.* 220 (2021), 117311.
- [15] A.F. Chadwick, P.W. Voorhees, The development of grain structure during additive manufacturing, *Acta Mater.* 211 (2021), 116862.
- [16] Q. Guo, M. Qu, C.A. Chuang, L. Xiong, A. Nabaa, Z.A. Young, Y. Ren, P. Kenesei, F. Zhang, L. Chen, Phase transformation dynamics guided alloy development for additive manufacturing, *Addit. Manuf.* 59 (2022), 103068.
- [17] Q. Chen, W. Xie, V.K. Champagne, A. Nardi, J.H. Lee, S. Müftü, On adiabatic shear instability in impacts of micron-scale Al-6061 particles with sapphire and Al-6061 substrates, *Int. J. Plast.* 166 (2023), 103630.
- [18] J.M. Flynn, A. Shokrani, S.T. Newman, V. Dhokia, Hybrid additive and subtractive machine tools—Research and industrial developments, *Int. J. Mach. Tools Manuf.* 101 (2016) 79–101.
- [19] W. Li, K. Yang, S. Yin, X. Yang, Y. Xu, R. Lupoi, Solid-state additive manufacturing and repairing by cold spraying: a review, *J. Mater. Sci. Technol.* 34 (2018) 440–457.
- [20] S. Bagherifard, J. Kondas, S. Monti, J. Cizek, F. Perego, O. Kovarik, F. Lukac, F. Gaertner, M. Guagliano, Tailoring cold spray additive manufacturing of steel 316 L for static and cyclic load-bearing applications, *Mater. Des.* 203 (2021), 109575.
- [21] S. Bagherifard, S. Monti, M.V. Zuccoli, M. Riccio, J. Kondás, M. Guagliano, Cold spray deposition for additive manufacturing of freeform structural components compared to selective laser melting, *Mater. Sci. Eng. A-Struct. Mater. Prop. Microstruct. Process.* 721 (2018) 339–350.
- [22] S. Pathak, G.C. Saha, Cold spray: its prominence as an additive manufacturing technology, in: S. Pathak, G.C. Saha (Eds.), *Cold Spray in the Realm of Additive Manufacturing*, Springer Cham, Switzerland, 2020, pp. 1–7.
- [23] G. Prashar, H. Vasudev, A comprehensive review on sustainable cold spray additive manufacturing: state of the art, challenges and future challenges, *J. Clean Prod.* 310 (2021), 127606.
- [24] M. Diab, X. Pang, H. Jahed, The effect of pure aluminum cold spray coating on corrosion and corrosion fatigue of magnesium (3% Al-1% Zn) extrusion, *Surf. Coat. Technol.* 309 (2017) 423–435.
- [25] T. Suhonen, T. Varis, S. Dosta, M. Torrell, J.M. Guilemany, Residual stress development in cold sprayed Al, Cu and Ti coatings, *Acta Mater.* 61 (2013) 6329–6337.
- [26] Y. Tao, T. Xiong, C. Sun, L. Kong, X. Cui, T. Li, G.L. Song, Microstructure and corrosion performance of a cold sprayed aluminium coating on AZ91D magnesium alloy, *Corrosion Sci.* 52 (2010) 3191–3197.
- [27] J.H. Martin, B.D. Yahata, J.M. Hundley, J.A. Mayer, T.A. Schaedler, T.M. Pollock, 3D printing of high-strength aluminium alloys, *Nature* 549 (2017) 365–369.
- [28] N.T. Aboulkhair, M. Simonelli, L. Parry, I. Ashcroft, C. Tuck, R. Hague, 3D printing of aluminium alloys: additive manufacturing of aluminium alloys using selective laser melting, *Prog. Mater. Sci.* 106 (2019), 100578.
- [29] H.R. Kotadia, G. Gibbons, A. Das, P.D. Howes, A review of Laser Powder Bed Fusion Additive Manufacturing of aluminium alloys: microstructure and properties, *Addit. Manuf.* 46 (2021), 102155.
- [30] R. Fu, Y. Guo, Y. Cui, J. Wang, H. Lei, C. Liu, Large-size ultra-high strength-plasticity aluminum alloys fabricated by wire arc additive manufacturing via added nanoparticles, *Mater. Sci. Eng. A-Struct. Mater. Prop. Microstruct. Process.* 864 (2023), 144582.
- [31] T. Paul, P. Nautiyal, C. Zhang, B. Boesl, A. Agarwal, Role of in-situ splat sintering on elastic and damping behavior of cold sprayed aluminum coatings, *Scr. Mater.* 204 (2021), 114125.
- [32] P. Nautiyal, C. Zhang, V.K. Champagne, B. Boesl, A. Agarwal, In-situ mechanical investigation of the deformation of splat interfaces in cold-sprayed aluminum alloy, *Mater. Sci. Eng. A-Struct. Mater. Prop. Microstruct. Process.* 737 (2018) 297–309.
- [33] N. Hutasoit, M.A. Javed, R.A. Rashid, S. Wade, S. Palanisamy, Effects of build orientation and heat treatment on microstructure, mechanical and corrosion properties of Al6061 aluminium parts built by cold spray additive manufacturing process, *Int. J. Mech. Sci.* 204 (2021), 106526.
- [34] B. Aldwell, E. Kelly, R. Wall, A. Amaldi, G.E. O'Donnell, R. Lupoi, Machinability of Al 6061 deposited with cold spray additive manufacturing, *J. Therm. Spray Technol.* 26 (2017) 1573–1584.
- [35] J.W. Murray, M.V. Zuccoli, T. Hussain, Heat treatment of cold-sprayed C355 Al for repair: microstructure and mechanical properties, *J. Therm. Spray Technol.* 27 (2018) 159–168.
- [36] S. Ngai, T. Ngai, F. Vogel, W. Story, G.B. Thompson, L.N. Brewer, Saltwater corrosion behavior of cold sprayed AA7075 aluminum alloy coatings, *Corrosion Sci.* 130 (2018) 231–240.
- [37] V. Champagne, D. Helfritch, The unique abilities of cold spray deposition, *Int. Mater. Rev.* 61 (2016) 437–455.
- [38] M. Kim, L.N. Brewer, G.W. Kubacki, Microstructure and corrosion resistance of chromate conversion coating on cold sprayed aluminum alloy 2024, *Surf. Coat. Technol.* 460 (2023), 129423.
- [39] P. Sirvent, M.A. Garrido, C.J. Munez, P. Poza, S. Vezzu, Effect of higher deposition temperatures on the microstructure and mechanical properties of Al 2024 cold sprayed coatings, *Surf. Coat. Technol.* 337 (2018) 461–470.
- [40] X. Pan, W. He, L. Zhou, S. Shu, X. Ding, Q. Wang, S. Wen, N. Li, M. Yi, Y. Zhu, J. Nan, Two laser beam modulation of microstructure and residual stress field in cold sprayed Al alloy for recovering fatigue performance, *Int. J. Plast.* 164 (2023), 103598.
- [41] T. Schmidt, F. Gärtner, H. Assadi, H. Kreye, Development of a generalized parameter window for cold spray deposition, *Acta Mater.* 54 (2006) 729–742.
- [42] I. Dowding, M. Hassani, Y. Sun, D. Veysset, K.A. Nelson, C.A. Schuh, Particle size effects in metallic microparticle impact-bonding, *Acta Mater.* 194 (2020) 40–48.
- [43] N. Fan, J. Cizek, C. Huang, X. Xie, Z. Chlup, R. Jenkins, R. Lupoi, S. Yin, A new strategy for strengthening additively manufactured cold spray deposits through in-process densification, *Addit. Manuf.* 36 (2020), 101626.
- [44] X. Luo, Y. Wei, J. Shen, N. Ma, C.J. Li, Breaking the trade off between corrosion resistance and fatigue lifetime of the coated Mg alloy through cold spraying submicron-grain Al alloy coatings, *J. Magnes. Alloy.* (2023). In Press.
- [45] B.L. James, V.S. Bhattiprolu, G.A. Crawford, B.K. Jasthi, Effect of zirconia secondary peening on the microstructure and mechanical behavior of Al6061 cold spray coatings, *Surf. Coat. Technol.* 436 (2022), 128269.
- [46] X.T. Luo, M.L. Yao, N. Ma, M. Takahashi, C.J. Li, Deposition behavior, microstructure and mechanical properties of an in-situ micro-forging assisted cold spray enabled additively manufactured Inconel 718 alloy, *Mater. Des.* 155 (2018) 384–395.
- [47] H. Zhou, C. Li, G. Ji, S. Fu, H. Yang, X. Luo, G. Yang, C. Li, Local microstructure inhomogeneity and gas temperature effect in in-situ shot-peening assisted cold-sprayed Ti-6Al-4V coating, *J. Alloy. Compd.* 766 (2018) 694–704.
- [48] D. Veysset, J.H. Lee, M. Hassani, S.E. Kooi, E.L. Thomas, K.A. Nelson, High-velocity micro-projectile impact testing, *Appl. Phys. Rev.* 8 (2021), 011319.
- [49] M. Hassani, D. Veysset, Y. Sun, K.A. Nelson, C.A. Schuh, Microparticle impact-bonding modes for mismatched metals: from co-deformation to splatting and penetration, *Acta Mater.* 199 (2020) 480–494.
- [50] M. Hassani-Gangaraj, D. Veysset, K.A. Nelson, C.A. Schuh, In-situ observations of single micro-particle impact bonding, *Scr. Mater.* 145 (2018) 9–13.
- [51] X. Wang, F. Feng, M.A. Klecka, M.D. Mordasky, J.K. Garofano, T. El-Wardany, A. Nardi, V.K. Champagne, Characterization and modeling of the bonding process in cold spray additive manufacturing, *Addit. Manuf.* 8 (2015) 149–162.
- [52] K. Yang, W. Li, X. Guo, X. Yang, Y. Xu, Characterizations and anisotropy of cold-spraying additive-manufactured copper bulk, *J. Mater. Sci. Technol.* 34 (2018) 1570–1579.
- [53] P. Gao, C. Zhang, R. Wang, G. Deng, J. Li, L. Su, Tamping effect during additive manufacturing of copper coating by cold spray: a comprehensive molecular dynamics study, *Addit. Manuf.* 66 (2023), 103448.
- [54] A.A. Hemeda, C. Zhang, X.Y. Hu, D. Fukuda, D. Cote, I.M. Nault, A. Nardi, V. K. Champagne, Y. Ma, J.W. Palko, Particle-based simulation of cold spray: influence of oxide layer on impact process, *Addit. Manuf.* 37 (2021), 101517.
- [55] Q. Wang, N. Ma, M. Takahashi, X. Luo, C. Li, Development of a material model for predicting extreme deformation and grain refinement during cold spraying, *Acta Mater.* 199 (2020) 326–339.
- [56] Q. Wang, N. Ma, X.T. Luo, C.J. Li, Towards better understanding supersonic impact-bonding behavior of cold sprayed 6061-T6 aluminum alloy based on a high-accuracy material model, *Addit. Manuf.* 48 (2021), 102469.
- [57] Q. Wang, N. Ma, X.T. Luo, C.J. Li, Capturing cold-spray bonding features of pure Cu from in situ deformation behavior using a high-accuracy material model, *Surf. Coat. Technol.* 413 (2021), 127087.
- [58] B. Yıldırım, H. Yang, A. Gouldstone, S. Müftü, Rebound mechanics of micrometre-scale, spherical particles in high-velocity impacts, *Proc. R. Soc. A-Math. Phys. Eng. Sci.* 473 (2017) 20160936.
- [59] S.M. Hassani-Gangaraj, K.S. Cho, H.J. Voigt, M.A. Guagliano, C.A. Schuh, Experimental assessment and simulation of surface nanocrystallization by severe shot peening, *Acta Mater.* 97 (2015) 105–115.
- [60] H. Liu, X. Xu, J. Zhang, Z. Liu, Y. He, W. Zhao, Z. Liu, The state of the art for numerical simulations of the effect of the microstructure and its evolution in the metal-cutting processes, *Int. J. Mach. Tools Manuf.* 177 (2022), 103890.
- [61] W. Zhang, X. Wang, Y. Hu, S. Wang, Predictive modelling of microstructure changes, micro-hardness and residual stress in machining of 304 austenitic stainless steel, *Int. J. Mach. Tools Manuf.* 130 (2018) 36–48.
- [62] B. Tekkaya, M. Meurer, M. Dötz, M. Könemann, S. Müntermann, T. Bergs, Modeling of microstructural workpiece rim zone modifications during hard machining, *J. Mater. Process. Technol.* 311 (2023), 117815.
- [63] H. Liu, J. Zhang, B. Xu, X. Xu, W. Zhao, Prediction of microstructure gradient distribution in machined surface induced by high speed machining through a coupled FE and CA approach, *Mater. Des.* 196 (2020), 109133.
- [64] Y. Hu, S. Wu, Y. Guo, Z. Shen, A.M. Korsunsky, Y. Yu, X. Zhang, Y. Fu, Z. Che, T. Xiao, S. Lozano-Perez, Inhibiting weld cracking in high-strength aluminium alloys, *Nat. Commun.* 13 (2022) 5816.
- [65] Y. Ichikawa, R. Tokoro, M. Tanno, K. Ogawa, Elucidation of cold-spray deposition mechanism by auger electron spectroscopic evaluation of bonding interface oxide film, *Acta Mater.* 164 (2019) 39–49.
- [66] R. Nikbakht, S.H. Seyedehin, S. Kheirandish, H. Assadi, B. Jodoin, Asymmetrical bonding in cold spraying of dissimilar materials, *Appl. Surf. Sci.* 444 (2018) 621–632.
- [67] H. Liu, K. Ushioda, H. Fujii, Elucidation of interface joining mechanism during friction stir welding through Cu/Cu-10Zn interfacial observations, *Acta Mater.* 166 (2019) 324–334.
- [68] A.A. Tiamiyu, C.A. Schuh, Particle flattening during cold spray: mechanistic regimes revealed by single particle impact tests, *Surf. Coat. Technol.* 403 (2020), 126386.